SCIENTIFIC REPORTS
nature research

OPEN

High pressure inhibits signaling protein binding to the flagellar motor and bacterial chemotaxis through enhanced hydration

Hiroaki Hata[1], Yasutaka Nishihara[2], Masayoshi Nishiyama[3], Yoshiyuki Sowa[4], Ikuro Kawagishi[4] & Akio Kitao[1*]

High pressure below 100 MPa interferes inter-molecular interactions without causing pressure denaturation of proteins. In *Escherichia coli*, the binding of the chemotaxis signaling protein CheY to the flagellar motor protein FliM induces reversal of the motor rotation. Using molecular dynamics (MD) simulations and parallel cascade selection MD (PaCS-MD), we show that high pressure increases the water density in the first hydration shell of CheY and considerably induces water penetration into the CheY-FliM interface. PaCS-MD enabled us to observe pressure-induced dissociation of the CheY-FliM complex at atomic resolution. Pressure dependence of binding free energy indicates that the increase of pressure from 0.1 to 100 MPa significantly weakens the binding. Using high-pressure microscopy, we observed that high hydrostatic pressure fixes the motor rotation to the counter-clockwise direction. In conclusion, the application of pressure enhances hydration of the proteins and weakens the binding of CheY to FliM, preventing reversal of the flagellar motor.

Pressure significantly affects protein structure, dynamics, and functions[1–4]. Very high pressure (above 500 MPa) induces denaturation of many soluble proteins[5–8], and therefore the mechanism of pressure denaturation has been relatively well investigated, both theoretically and experimentally[4,9,10]. On the other hand, pressures below 100 MPa, a range that covers the typical biosphere on earth, including the deep sea, does not induce large changes in overall secondary and tertiary structure of most protein molecules[1,3,11,12], but was found to affect behaviors of biological systems at macroscopic levels[13–15]. Pressures of ~ 100 MPa are known to interfere with interactions between biomolecules such as proteins and ligands[1,4,14,16,17], indicating that the mechanism whereby high pressure perturbs such interactions should be elucidated at the molecular level.

Molecular dynamics (MD) simulation has been applied to obtain atomic details of structures and functions of biomolecules, including surrounding water and other molecules[18–20]. MD simulations under high pressures have observed enhanced hydration of proteins[21–23] and penetration of water molecules inside proteins with accompanying conformational changes[24,25]. However, it remains difficult to simulate pressure effects on protein-protein interactions, given that the timescale for observing the pressure effects is often longer than the length of typical MD simulations[4,26]. Recently, a new distributed computing method, parallel cascade selection molecular dynamics (PaCS-MD), has been developed to observe events whose timescales are longer than the standard MD length[27,28]. PaCS-MD can simulate dissociation process of protein complexes, whose time scales range from μs to s, without using artificial forces within a short MD simulation time[29]. Additionally, by integrating the distributed MD trajectories using a Markov state model (MSM)[30], various quantities characterizing molecular interactions can be calculated, such as binding free energy, association/dissociation rate constants, and residence times[29,31].

In the present study, we investigate the effect of high pressure on the interactions between the chemotaxis signaling protein CheY and the flagellar rotor protein FliM by a combination of MD, PaCS-MD/MSM, and high-pressure microscopy. Switching of the bacterial flagellar motor from counter-clockwise (CCW) to clockwise (CW) is triggered by the binding of the phosphorylated CheY (CheYp) to the N-terminal segment of FliM

[1]School of Life Science and Technology, Tokyo Institute of Technology, Ookayama, 2-12-1 Meguro-ku, Tokyo, 152-8550, Japan. [2]Institute of Molecular and Cellular Biosciences, The University of Tokyo, 1-1-1 Yayoi, Bunkyo-ku, Tokyo, 113-0032, Japan. [3]Department of Physics, Kindai University, 3-4-1 Kowakae, Higashiosaka, Osaka, 577-8502, Japan. [4]Department of Frontier Bioscience, Hosei University, Koganei, Tokyo, 184-8584, Japan. *email: akitao@bio.titech.ac.jp

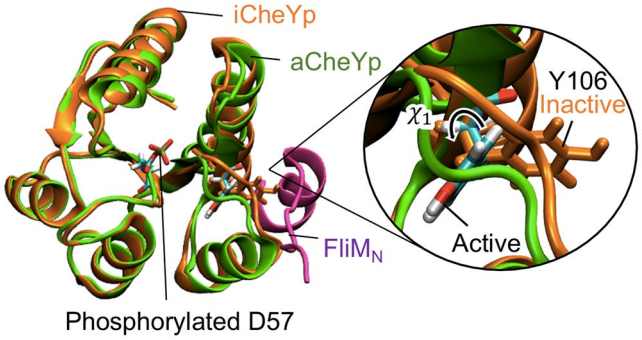

Figure 1. Molecular structures of CheYp and $FliM_N$. Initial MD structures of the phosphorylated CheY in the active (aCheYp: green) and inactive (iCheYp: orange) forms. Y106 and the phosphorylated D57 residues are shown in stick models and those of aCheYp are colored on an atomic-color basis. A close-up view of Y106 is shown on the right. The $FliM_N$ structure complexed with aCheYp is shown in magenta. In this paper, the molecular structure was visualized using VMD[82].

($FliM_N$)[32,33], which is essential for bacterial chemotaxis[34]. During CCW rotation, multiple flagellar filaments form a bundle, which smoothly propels the bacteria; in contrast, CW rotation untangles the bundle and consequently leads to changes in the swimming direction. This switching was investigated based on the four-state model of a protomer as the combination of CheYp-bound/unbound state and active/inactive conformation[35–37]. High-pressure microscopy has revealed various phenomena induced in the flagellar motor by pressure[15,38]. *Escherichia coli* cells stop swimming at 80 MPa even if the flagellar motors generate sufficient torque, which implies the inhibition of flagellar bundle formation[38]. Application of pressure >120 MPa induces a reversal from CCW to CW in the absence of CheYp, suggesting pressure-induced structural changes similar to those caused by the binding of CheYp[15]. At the molecular level, however, high-pressure effects on the CheYp–FliM binding have not been fully explored.

To investigate the CheYp–FliM interaction, we first examine the protein structure of CheY and $FliM_N$ at pressures up to 100 MPa by standard MD simulations, which identify changes in the protein structures and the hydration state induced by high pressure. We then use PaCS-MD to simulate the high-pressure dissociation process of the CheYp-$FliM_N$ complex, demonstrating that pressure increased hydrated waters and enhanced penetration of water molecules into the complex interface. MSM analysis quantitatively shows that high pressure decreases the binding free energy between CheYp and $FliM_N$. This tendency is consistent with the microscopic observations, which showed that high hydrostatic pressure exclusively fixes the motor rotation in the CCW orientation at 40 MPa. We conclude that the application of pressure enhances hydration of the proteins and weakens the binding of CheYp to $FliM_N$, resulting in CCW rotation of the flagellar motor.

Results and Discussion

CheYp active form is stable even at high pressure. First, we examined the pressure effects on phosphorylation-dependent stability of monomeric CheY active form by MD simulation. Phosphorylation of CheY at the Asp57 sidechain induces a conformational change of CheY from the inactive (Fig. 1, orange) to the active (Fig. 1, green) form that is mainly characterized by a transition of the sidechain χ_1 angle of Tyr106 from ~ 60° to ~ −150°[39,40], resulting in an increase in the binding affinity of CheY for the N-terminal segment of FliM ($FliM_N$)[39,41]. To model the combination of the inactive (Tyr106 χ_1 ~ 60°) or active (~−150°) form, phosphorylated (CheYp) or non-phosphorylated at Asp57 (CheY), four different models of CheY (aCheYp, iCheYp, aCheY, and iCheY) were constructed and simulated for 1 μs by MD at 0.1 and 100 MPa.

In the MD simulations of CheYp started from the active form (aCheYp: $\chi_1 = -150°$), χ_1 remained at approximately −150° at both 0.1 and 100 MPa (upper panel in Fig. 2a). Even when the MD of CheYp was started from the inactive form (iCheYp: $\chi_1 = 60°$), χ_1 angle made a transition from 60° to −150° and remained at approximately −150° at both pressure conditions (second upper panel in Fig. 2a). The calculated free energy of the inactive form compared to the active form (ΔG_M) was higher than that of the active form by a few kcal/mol when CheY is phosphorylated (Table S1). These results clearly indicated that, for CheYp, the active form is more favorable than the inactive form in the pressure range ≤100 MPa. The observed stabilization of phospho-CheY in the active form at ambient pressure is consistent with previous experimental observations[42–44]. It is worth mentioning that the time scale of the active-inactive transition is slowed at 100 MPa. In the case of iCheYp, the transition at 100 MPa occurred after 120 ns, while this transition was observed within 20 ns at 0.1 MPa. The same trend was also seen in the other cases. This slowing presumably reflects the pressure-induced slowdown of molecular motion and a consequent stiffening[45–47].

In the case of non-phosphorylated CheY, the active form is more destabilized. Non-phosphorylated CheY (lower two panels of Fig. 2a) tended to make conformational transitions between the active and inactive forms, with the exception of iCheY at 0.1 MPa. Starting from the active form without phosphorylation (aCheY) at 0.1 MPa, CheY exhibited conformational transitions between the two forms and eventually shifted predominantly to the inactive form, while at 100 MPa, CheY mostly remained in the active form; this pattern presumably resulted the slowed conformational change at high pressure. MD of non-phosphorylated CheY started from the inactive (iCheY) underwent no such transition and retained the inactive form at 0.1 MPa; few transitions were

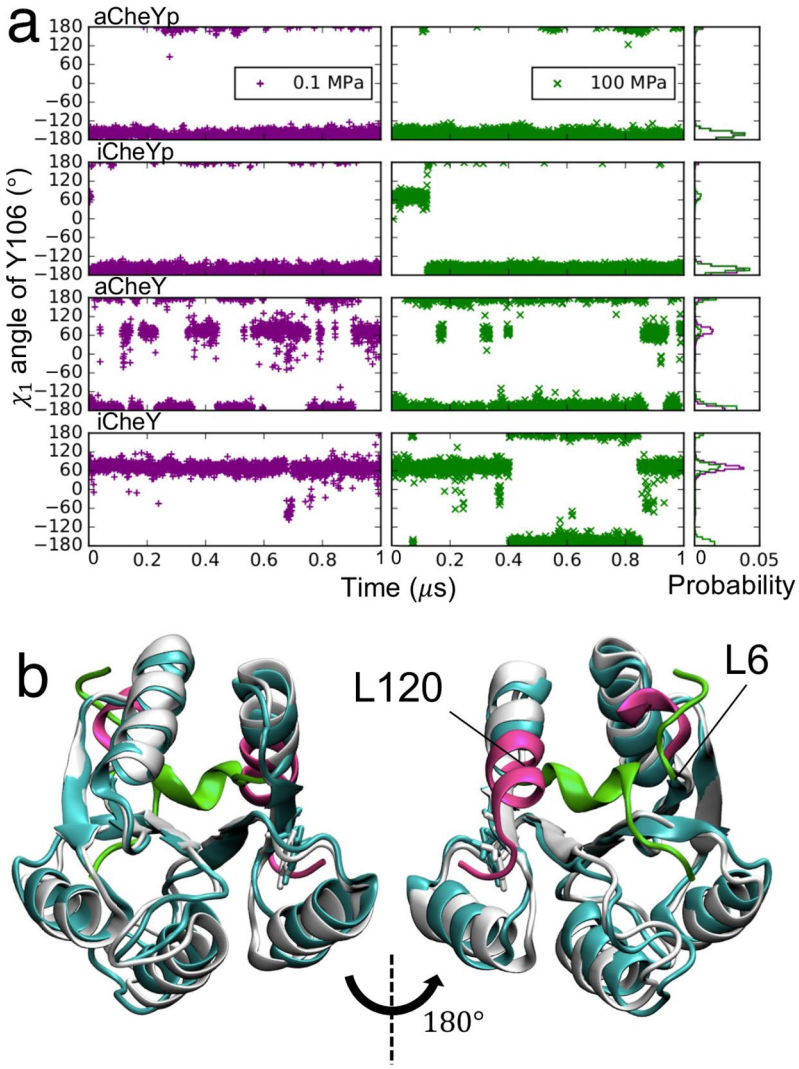

Figure 2. Pressure effects on the CheY monomer. (**a**) Time evolution of the χ_1 angle of Y106 during the 1-μs MD simulations for four different models of CheY at 0.1 (purple) and 100 MPa (green). Probability densities are shown on the right. (**b**) Representative structures of aCheYp at 0.1 (white) and 100 MPa (cyan). A view from the opposite side is shown on the right. Segments significantly affected by pressure are shown in a different color, with the structures at 0.1 and 100 MPa indicated in magenta and green, respectively. Residues on the edges of the segments that underwent conformational transitions are labeled. The representative structures were determined as cluster centers by the k-means clustering of the last half of the MD trajectories.

observed at 100 MPa. The free energy difference ΔG_M was significantly dependent on the initial form unlike that of the phosphorylated CheY (Table S1). Overall, the MD simulation of monomeric CheY clearly indicated that activated phospho-CheY is not affected by high pressure below 100 MPa.

Pressure causes significant conformational change of CheY at 100 MPa. In the case of aCheYp at 100 MPa, we observed an interesting conformational transition of the N- and C-terminal segments during MD (Fig. 2b); this transition began at approximately 0.5 μs and was completed at approximately 0.74 μs. The N-terminal conformational change involved the first five residues of CheY, a region that is far from the $FliM_N$-binding site; the C-terminal conformational change occurred as a significant bending of the helix caused by large mainchain dihedral changes in Lys119 and Leu120, as revealed by Dihedral Transition Analysis (DTA)[48]. Since CheY residues 122, 123, and 126 are part of the interface residues of the complex, the binding affinity may be weakened by loss of some interactions if this conformational transition occurs upon binding; however, the bending occurred in the direction opposite to the $FliM_N$-binding site (compare Figs. 1a and 2b), and this conformation is not expected to sterically interfere with $FliM_N$ binding. In iCheY, a similar N-terminal change in the first five residues was observed at 100 MPa. In addition, we also identified a "sidechain flip"[48] of Asp74, situated in at the end of the α-helix and far from the $FliM_N$-binding interface.

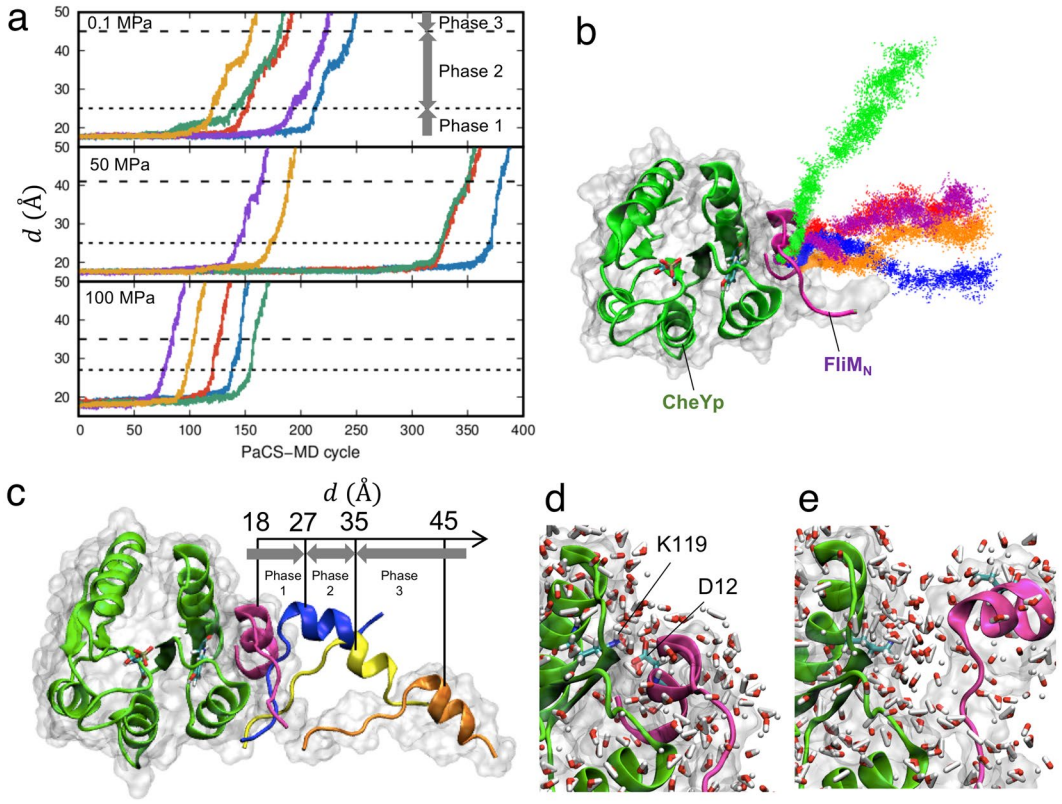

Figure 3. Dissociation of the CheYp–FliM$_N$ complex at 0.1, 50, and 100 MPa, as simulated by PaCS-MD. (**a**) The inter-COM distance between CheYp and FliM$_N$, with d indicated as a function of the PaCS-MD cycle at 0.1 (top), 50 (center), and 100 (bottom) MPa. Five independent PaCS-MD simulations are shown in different colors. The broken lines indicate the borders between Phases 1–2 and 2–3. (**b**) COM positions of FliM$_N$ obtained by PaCS-MD and all additional MD simulations at 100 MPa. Color differences denote different trials. (**c**) Examples of snapshots of FliM$_N$ during a dissociation at 100 MPa. MD snapshots with four different d values are shown in different colors after superimposing CheYp. Molecular surfaces of the initial and last snapshots are shown in transparent colors. (**d,e**) Closeup view of the interface, (**d**) before the breakage of the key salt bridge (Lys119: CheY–Asp12: FliM$_N$) at $d = 18$ Å, and (**e**) just after the detachment of the FliM$_N$ helix at $d = 27$ Å at 100 MPa. Water molecules in the first hydration shell of each protein are shown with stick models and atomic-color basis.

Pressure induces earlier detachment of FliM$_N$. Next, we investigated pressure effects on the aCheYp–FliM$_N$ complex by 1-μs MD at 0.1, 50, and 100 MPa. During the 1-μs MD, the complex structure was stable and its dissociation was not observed. Experimentally, dissociation of some protein complexes has been shown to occur at ~ 60 MPa[14,49], but simulating the dissociation process using standard MD is very difficult because the time scale of the complex dissociation can be much longer than the MD time scale[26]. Some of the residues between residues 83–125 of CheY make contacts with FliM$_N$. The complex structure is stabilized by a salt bridge between Lys119 of CheY and Asp12 of FliM$_N$ (Fig. S1) that was maintained during 90% of the simulation time, and also by a few mainchain–sidechain hydrogen bonds. Since the aforementioned conformational transition at 100 MPa starts from Lys119, that change may weaken the binding if the transition occurs. However, such a conformational change was not observed in the simulation of the complex at high pressure nor in the following dissociation simulations.

The dissociation process of the aCheYp and FliM$_N$ complex was observed by PaCS-MD at 0.1, 50, and 100 MPa. In the present work, we focused on examining the pressure dependence of the binding affinity; five PaCS-MD trials were sufficient for this purpose, as will be shown below. In all the trials, dissociation up to 50 Å in the inter-center of mass distance, d, was observed within 400 cycles (Fig. 3a). This computational cost corresponds to a total simulation time of 40 ns (0.1 ns MD per replica × 400 cycles) and total computational cost of 400 ns (40 ns × 10 replicas). Relatively large variations in the number of PaCS-MD cycles required to cause the dissociation were consistent with the results of the earlier paper[31], which showed that this number varied in different trials when 10 replicas were used. The generated dissociation pathways are shown in Fig. 3b,c, and in Movies S1-S3. Although the direction of dissociation varied, the helical segment of the C-terminal segment of FliM$_N$ always detached from aCheYp first, with subsequent unbinding of the N-terminal region (Fig. 3c–e). The former step, consisting of detachment of the FliM$_N$ C-terminal helix, occurred at $d = 25 \pm 2$, 25 ± 2, and 27 ± 2 Å at 0.1, 50, and 100 MPa (mean ± standard deviation (SD)), respectively, indicating a lack of clear pressure

dependence. This process correlated with breaking of the aforementioned salt bridge (Lys119: CheY–Asp12: $FliM_N$), which occurred slightly earlier at $d = 20 - 21$ Å. The subsequent unbinding of the N-terminal region occurred at $d = 45 \pm 3$, 41 ± 3, and 35 ± 4 Å at 0.1, 50, and 100 MPa, respectively, suggesting that higher pressure induces earlier complete detachment of $FliM_N$. We regard the phase before the helix detachment as the bound state (Phase 1), the phase before the complete dissociation as the partially bound state (Phase 2), and the last phase as the unbound state (Phase 3). This pressure-dependent dissociation is investigated further below.

In addition, we examined pressure effects on monomeric $FliM_N$ by analyzing MD trajectories generated by two different procedures. In the first procedure, MD simulations were started from the $FliM_N$ structure taken from the crystal structure of the complex (PDB ID: 1F4V[39]) and solvated as a monomer. MDs lasting 1 μs were conducted at 0.1, 50, and 100 MPa and analyzed. In the second procedure, the $FliM_N$ structures completely dissociated from aCheYp ($d > 40$ Å) by PaCS-MD were analyzed. $FliM_N$ in the former tended to maintain the helical region formed in the CheY-bound state, whereas in the latter, $FliM_N$ was slightly more unstructured in the helical region, a change that was induced during the detachment process.

Thermodynamic properties of the proteins are conserved up to 100 MPa. Various properties of $FliM_N$ and aCheYp in monomeric and complex states were calculated at different pressures (Table S2). The root-mean-square deviation (RMSD) of α-carbons (C_α) of the MD-representative structure at high pressures compared to that at 0.1 MPa was small (~1 Å) for monomeric CheY and the aCheYp–$FliM_N$ complex, except for monomeric aCheYp and iCheY at 100 MPa, in which the aforementioned conformational changes occurred. The RMSD of monomeric $FliM_N$ is larger, mainly due to the structural fluctuation of the unstructured segment at the N-terminus, which is also very flexible in the complex form. In the helical region of $FliM_N$ (residues 8–15), the RMSD was much smaller. These results indicated that hydrostatic pressures up to ~50 MPa do not significantly change the structures of the monomers and complex within the range of the simulations, but suggested that 100-MPa pressure can change the structure of monomeric CheY. The solvent accessible surface area (SASA) and the excluded volume (V_{ex}), the cavity volume (V_{cav}), and the isothermal compressibility (κ_T) also showed no significant change between the two pressure conditions (Table S2). It is worth mentioning that the TIP3P model[50] used in the current simulation has been reported to reproduce experimental compressibility up to 200 MPa[51]. Since CheY is a small protein, the V_{cav} of CheY was very small even at 0.1 MPa and shrank slightly at 100 MPa; however, the amount of shrinkage was equivalent only to the size of one water molecule, which is smaller than the observed cavity and volume fluctuations. The pressure-independent behavior of κ_T is consistent with the fact that protein structure does not significantly change in this pressure range, indicating that high pressure mainly compresses water. This result is considered to be reasonable, given that the κ_T of bulk water is ~ 2-fold larger than that of typical proteins[10,52]. This observation also is consistent with the Young's moduli of hydrated proteins, which are in the range of 1 ~3 GPa for actin, tubulin, and flagellin[53]. The Young's modulus of CheY should be equal to or greater than those of these proteins, given that CheY is a smaller and more-compact globular protein. Expected elastic deformation at 100 MPa should be 3.3% if Young's modulus is 3 GPa, which suggests very small deformation comparable to thermal fluctuations (~1Å).

Pressure increases protein hydration and induces water penetration into the interface. Next, we analyzed the hydrogen bond network, including water molecules. The applied pressure did not alter the number of hydrogen bonds connecting protein-protein (H_{PP}) that sums up both intra- and inter-protein hydrogen bonds (Table S2). The result is consistent with the aforementioned result that high pressure ≤ 100 MPa does not change protein structure in most cases. Similarly, the number of protein-water-protein hydrogen bond network (H_{PWP}) was almost pressure-invariant. On the other hand, the number of protein-water hydrogen bonds (H_{PW}) in monomeric CheY and the complex increased as the pressure increased, which agrees with the expectation that high pressure results primarily in the compression of water. Similar changes in the hydrogen bonding network at the protein-water interface previously have been reported to be induced by pressure[23].

Next, we investigated water molecules in the first and second hydration shells around the proteins, namely the first and second shell surface waters, which are defined as the water molecules within 3 and 3–6 Å (respectively) from any protein atoms. We counted the number of surface waters in the first and second shells, N_{1SW} and N_{2SW}, respectively. Interestingly, significant increases in hydrated water molecules at high pressure were observed (Fig. 4a), consistent with the aforementioned increase in H_{PW} (Table S2). Compared to 0.1 MPa, ~ 30 more water molecules were found in the first hydration shell of monomeric CheY and the aCheYp–$FliM_N$ complex at 100 MPa, which is equivalent to ~ 8% increase in the ratio (r_{1SW}). This increase was slightly higher than the average increase in the density of bulk water at the increased pressure (~5%). Bulk water densities at 0.1, 50, and 100 MPa were calculated to be 3.29 ± 0.70, 3.37 ± 0.69, and $3.45 \pm 0.67 \times 10^{-2}$ Å^{-3}, respectively (see Methods for detail). These results indicated that the pressure increase induces an increase of water density around the protein surfaces compared to that of bulk water. This observation is consistent with previous theoretical and experimental studies of proteins in solution at similar pressures[1,3,11,21]. This tendency of hydration increase at higher pressure also was seen in the second hydration shell (~6% increase in r_{2SW}) but the increase was nominally less than that seen in r_{1SW}. The increase of hydration water was exceptionally higher for aCheYp in the monomernic state at 100 MPa, in which (as mentioned earlier) a conformational transition of the C-terminal helix was seen. The same tendency also was observed in the number of interface waters, which was analyzed as described below. This observation implied that the conformational transition promotes greater hydration of aCheYp at higher pressure.

We further focused on hydration around the complex interface and conducted similar analysis of the number of interface water in the first (N_{1IW}) and second (N_{2IW}) hydration shells around the interface residues (Table S2). These residues are defined as the residues involved in CheYp-$FliM_N$ contacts during more than 80% of the time of the second half of the 1-μs MD trajectory at 0.1 MPa. As expected, the increase in N_{1IW} was significant in all cases. For example, the water density of the interface in the first shell in the complex increased 6% when comparing

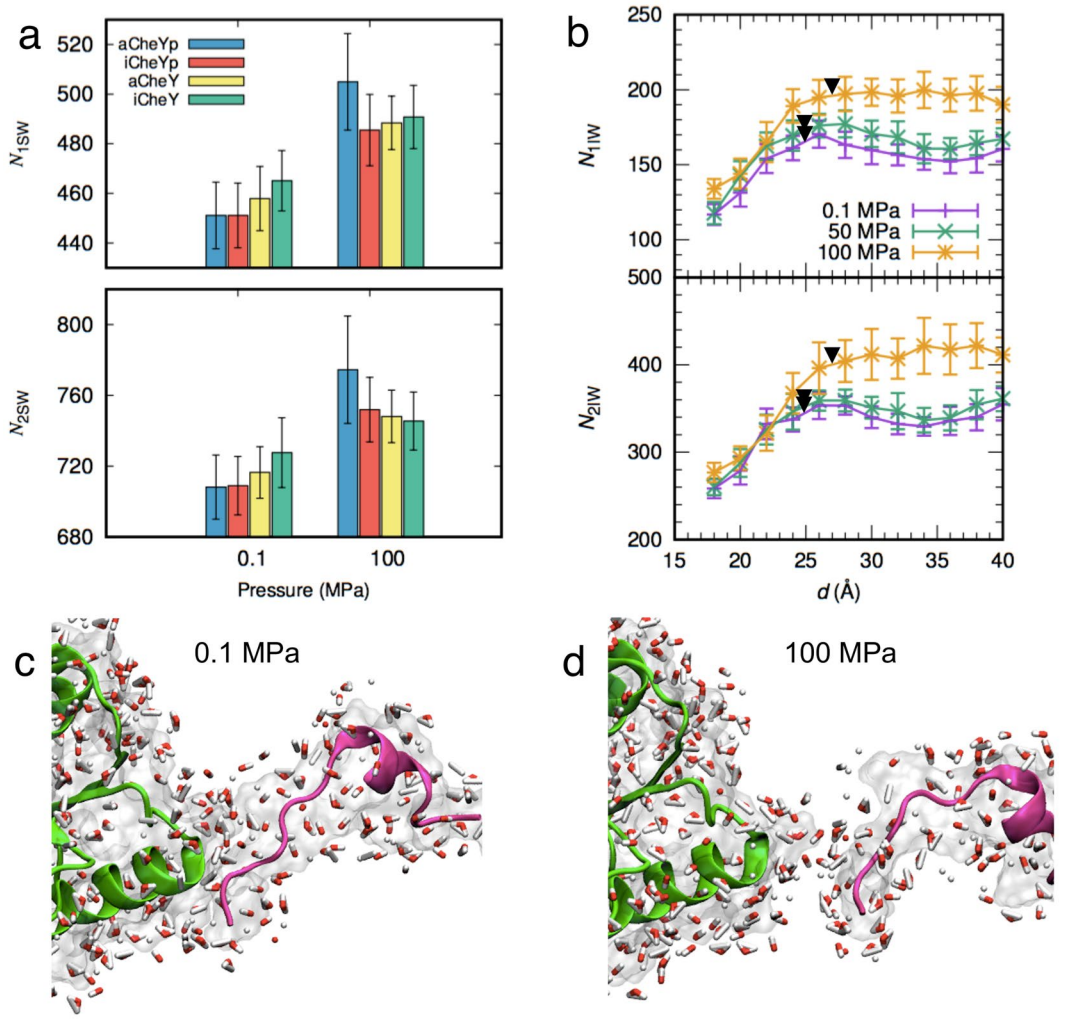

Figure 4. Pressure effects on protein hydration. (**a**) Pressure dependence of the number of surface waters in the first and second shells, N_{1SW} (upper panel) and N_{2SW} (lower panel), respectively. (**b**) Change in the numbers of interface waters, N_{1IW} (upper panel) and N_{2IW} (lower panel), during the dissociation process along d at 0.1 (purple), 50 (green), and 100 MPa (orange). The error bars show standard deviations among the five dissociation simulations. Black triangles indicate the borders between Phases 1 and 2. (**c,d**) MD snapshots at $d = 40$ Å at (**c**) 0.1 or (**d**) 100 MPa. Molecular representation is the same as in Fig. 3c,d.

between 0.1 MPa and 50 MPa, and 8% when comparing between 0.1 MPa and 100 MPa (see r_{1IW} in Table S2), while those of the second shell increased 5% and 4%, respectively (see r_{2IW} in Table S2). This result also showed that, in both the protein surface and protein-protein interface, the first shell water density tends to increase more than that of the second shell. High pressure increases the water density of the first hydration shell around the proteins and provokes water penetration into the interface. As shown above, high pressure did not change the timing of the salt bridge breakage, which implied that high pressure has a relatively weak effect on the salt bridge stability. Once salt bridge breakage occurred in the initial stage of dissociation, enhanced water penetration at high pressure accelerated the complete dissociation.

During the dissociation process of the complex, N_{1IW} and N_{2IW} gradually increased until the detachment of the C-terminal helix of aCheYp at the end of Phase 1, which is indicated by triangles in Fig. 4b. At this moment, the number of interface waters at 100 MPa was significantly greater than those at 0.1 and 50 MPa, which indicates the nonlinearity of the high-pressure effect on hydration at the protein-protein interface. As noted above, complete dissociation occurred at shorter d as pressure increased. This acceleration was caused by the increased hydration at higher pressure (Fig. 4c,d). At 0.1 MPa and $d = 40$ Å, the complex was still in Phase 2 (Fig. 4c) but completely dissociated at the same distance at 100 MPa because more water molecules penetrated into the complex interface (Fig. 4d).

Pressure impairs CheYp–FliM$_N$ binding. The free energy profile (potential of mean force as a function of d) from the bound to unbound states of CheYp and FliM$_N$ at 0.1, 50, and 100 MPa was calculated using the MSM analysis of the MD trajectories and is shown in Fig. 5a. This showed that the free energy difference between the bound and unbound states significantly decreases as the pressure increases, which clearly indicates weaker

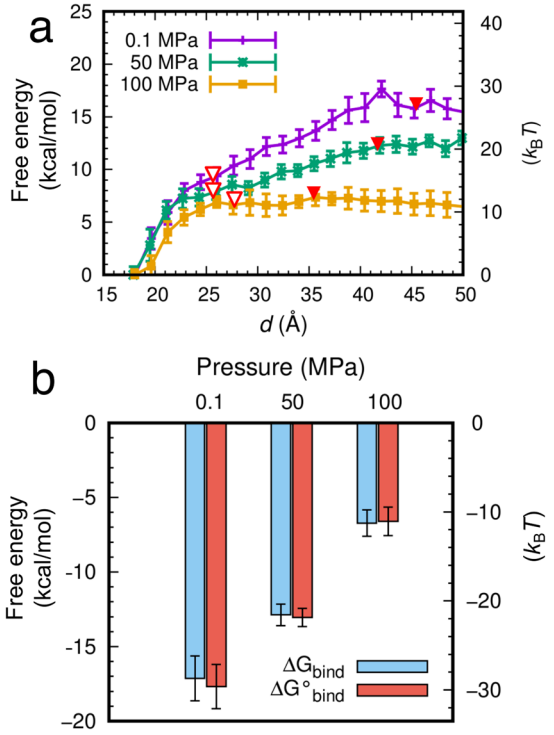

Figure 5. Pressure effects on binding free energy. (**a**) Dissociation free energy profiles as a function of d calculated by PaCS-MD/MSM. Red open and filled triangles indicate the borders between Phases 1–2 and 2–3, respectively. (**b**) Standard binding free energies calculated from the free energy profiles and volume correction (ΔG°_{bind}) and binding free energies before volume correction (ΔG_{bind}).

binding affinity at higher pressure. Although only five PaCS-MD trials were conducted, the free energy profiles showed small standard deviations, indicating that free energy converges to a certain value independent of dissociation direction if two molecules are sufficiently separated and interactions between the molecules become negligibly small, as shown in earlier work[29,31]. It should be noted that the free energy converged upon complete detachment of the complex, shown by red triangles in Fig. 5a. Since free energy differences among different pressures in Phase 1 (up to red open triangles) also were relatively small, the overall free energy differences originated mainly from the changes that occurred in Phase 2. From the point of view of the free energy profile, this difference may be interpreted as the result of weakened long-range interactions between the two proteins by more hydrated waters infiltrating between the proteins at higher pressure.

The standard binding free energy ($\Delta G^{\circ}_{\mathrm{bind}}$) of aCheYp and $\mathrm{FliM_N}$ was calculated from the free energy profile (see Methods) and is shown in Fig. 5b. The $\Delta G^{\circ}_{\mathrm{bind}}$ value significantly decreased with an increase of hydrostatic pressure. This observation is qualitatively consistent with the model that protein-protein binding is suppressed by hydration of protein surfaces induced by high hydrostatic pressure[1]. The change in the $\Delta G^{\circ}_{\mathrm{bind}}$ value from 50 to 100 MPa (6.5 kcal/mol) was greater than that from 0.1 to 50 MPa (4.6 kcal/mol), which is consistent with the non-linear pressure response shown above. Overall, the simulation results suggested that the binding affinity of the CheYp protein to the flagellar motor protein FliM is significantly lowered by high pressure.

Pressure inhibits CW rotation of *E. coli* flagellar motors. Finally, we experimentally examined the effect of hydrostatic pressure on the rotation of the flagellar motor in *E. coli* strain SYC12 (wild type for chemotaxis) by high-pressure microscopy. Rotation of a single motor was monitored as rotation of a cell body by attaching a single flagellar filament extended from the cell body directly to an inserted coverslip in the high-pressure chamber (Fig. 6a). Figure 6b shows typical time courses of the rotational speed of a single motor at 0.1 and 40 MPa, respectively. At 0.1 MPa, the flagellar motor rotated smoothly, and the rotational direction frequently switched from CCW to CW, and vice versa. In contrast, the motor rotated exclusively in a CCW direction at 40 MPa. The CW bias values, the time occupancy of CW rotation, at 0.1 and 40 MPa were 0.19 and zero, respectively ($n = 25$ cells) (Fig. 6c). On the other hand, application of 40 MPa showed no significant effect on the rotational speed (Fig. 6d). After the release of pressure, the frequent switching of the motor was observed to resume. These results indicated that application of 40 MPa of pressure suppresses motor switching, without affecting the overall structure and function of the motor. Therefore, the application of pressure is suggested to inhibit the binding of CheYp to FliM in *E. coli* cells, which is consistent with our observations using the simulations.

The bacterial switch complex in *E. coli* is a large ring comprising ~34 FliM proteins[54]. To understand how this large complex can instantaneously switch the conformations between CCW and CW rotations, the conformational spread model was proposed[35,55]. This cooperative model allows for a multistate switch in which each protomer switches its conformation non-instantaneously by biased random walk between conformational states

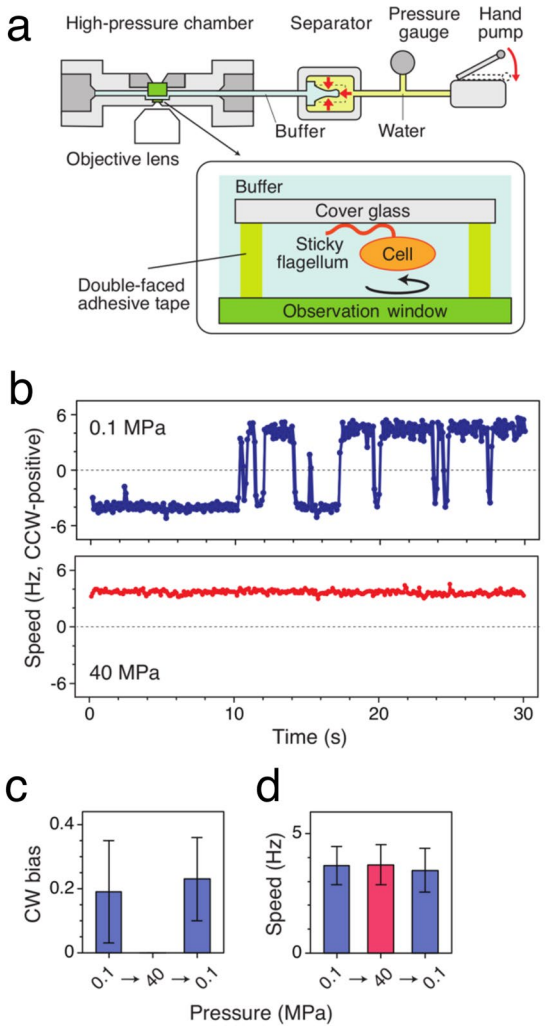

Figure 6. Rotation of flagellar motors at high pressure. (**a**) Schematic illustration of the experimental setup. (**b**) Time courses of the rotational speed of the same motor of the *E. coli* strain (wild type for chemotaxis) at 0.1 (top) and 40 MPa (bottom). (**c**,**d**) Pressure response of the rotational directionality (**c**) and speed (**d**). The rotation of the same motors was tracked when the pressure was changed from 0.1 to 40 MPa, and then returned to 0.1 MPa (mean ± SD, $n = 25$).

with broadly distributed durations. Since the binding of CheYp to $FliM_N$ affects the inter-molecular interactions between FliM proteins[56], the high-pressure inhibition of the binding is expected to reduce the probability to initiate the conformational switch to CW rotation, and also increase the probability to back to CCW rotation.

Compared to the typical time scale of the switching, the monomeric binding of CheYp to $FliM_N$ may be too strong (~30 k_BT). For example, typical duration of CW rotation is ~ 0.1 s but the dissociation rate constant k_{off} estimated with the transition state theory is 0.6 s^{-1} (The Eyring equation, $k_{off} = k_BT/h \exp(-\Delta G°_{bind}/RT)$, was used with $\Delta G°_{bind} = 30\ k_BT$. R and h are gas and Planck's constants, respectively). One possible explanation for the time scale gap is inaccurate estimation of this method. Since $\Delta G°_{bind}$ is related to k_{off}, k_{on} (association rate constant) and K_d (dissociation constant) with $K_d = k_{off}/k_{on} = C_0 \exp(\Delta G°_{bind}/k_BT)$ ($C_0 = 1$ molar), the value of k_{off} can have significant variations depending on k_{on} with a fixed value of $\Delta G°_{bind}$. Another possible explanation may be also related to the results that protein-protein K_d measured *in vivo* are one to three order greater than those *in vitro*[57], suggesting that the protein-protein binding *in vivo* can be significantly weaker than that *in vitro*. The other possible reason is overestimation of $\Delta G°_{bind}$ in this study, however, the previous two applications of the same calculation procedure reproduced experimental binding free energy well within the error of 1 kcal/mol[29,31], implying that the calculation error in this work is also not large. Finally, the aforementioned collective nature of the switch complex might be also related to the time gap.

Conclusion

In this work, we first showed, by MD simulation, that the binding of chemotaxis signaling protein CheYp to motor rotor protein $FliM_N$ is inhibited at high pressure. Even at 100 MPa, the active form of CheYp was shown to retain its overall structure at ambient pressure, but high pressure increased the water density in the first hydration shell and caused conformational change of the C-terminal helix in the monomeric aCheYp case. Using dissociation

simulation of the CheYp–FliM$_N$ complex by PaCS-MD and subsequent MSM analysis, we demonstrated that the binding affinity of the two proteins weakens as pressure rises, as shown by the calculated standard binding free energy. Consistent with these results, we showed, by high-pressure microscopy, that high pressure reversibly suppresses CW rotation of the bacterial flagellar motor. Altogether, our results provide a clear picture of high-pressure inhibition of CheYp–FliM$_N$ binding.

To the best of our knowledge, this is the first molecular simulation that observed the pressure-induced dissociation process of protein complexes in solution without applying bias. Since the calculation of binding free energy between proteins requires very long computational time, the pressure dependence of the binding free energy between proteins previously has been argued based on calculations for smaller methane-like molecules[58,59]. According to the heteropolymer collapse theory, hydrophobic interactions are destabilized by pressure far above 100 MPa, where the pressure-induced change in the interfacial free energy between protein and water lead to the penetration of water into a protein's hydrophobic core and result in protein denaturation[60]. In the present work, we demonstrated that the binding free energy between protein molecules decreases as pressure increases in the range $\leq$100 MPa. High pressure in this range induces a significant increase of water density around proteins; this increase is higher than that of bulk water density, especially in the first hydration shell, which apparently facilitates water penetration into the protein complex interface. We also observed a breakage of a key salt bridge accompanied by dissociation of the protein complex. Water molecules around such broken ionic bonds have been known to form a hydration shell that has a higher packing density than that of bulk water (i.e., electrostriction), which decreases the volume of a system and favors rupture of ionic bonds at high pressure[61].

In conclusion, high pressure modulates a protein-protein interaction by changing its hydration state even at 100 MPa or below. This pressure range is equivalent to the pressure in the deep sea, although studies for pressure effects on proteins have focused primarily on the denaturation (or unfolding) of proteins caused by higher pressures[4,9,61]. Studies on the effects of such relatively high pressure on proteins in the biosphere are essential for understanding proteins' bioresponsive functions at the molecular level and also for designing functions governed by protein-protein interactions.

Materials and Methods

MD simulation of monomeric CheY, FliM$_N$, and the complex. First, pressure effects on monomeric CheY, monomeric FilM$_N$, and their complex were investigated by standard MD simulation. We prepared four different models of CheY (aCheYp, iCheYp, aCheY, and iCheY). The structure of aCheY was generated by removing FliM$_N$ from the aCheY-FliM$_N$ complex structure (PDB ID: 1F4V[39]). The monomeric CheY crystal structure (PDB ID: 3CHY[40]) was used for iCheY. The aCheYp and iCheYp structures were generated by modeling the phosphorylated Asp57 residue based on the crystal structure of an α-thiophosphonate derivative of the CheY D57C point mutant (PDB ID: 1C4W[42]). The N-terminal fragment (residues 1–16) of the monomeric FliM$_N$ was obtained by removing aCheY from the crystal structure of the complex. The crystal structure of BeF_3^--activated CheY in complex with FliM$_N$ comprising residues 1–16 shows that the first 7 residues of FliM$_N$ takes an extended conformation and residues 8–15 forms an α-helix[39]. The CheYp–FliM$_N$ complex structure was modeled based on the crystal structure (PDB ID: 1F4V[39]) by replacing BeF_3^- with a phosphate group.

After energy minimization, each of the above protein models was solvated into a cubic periodic box and gaps were filled with water molecules and 0.15 M KCl. The prepared systems contain a total of ~ 34,000, 23,000 and 38,000 atoms for monomeric CheY, monomeric FliM$_N$, and the CheYp–FliM$_N$ complex, respectively. All of the MD simulations were performed using the GPU implementation[62] of the PMEMD module of the Amber14 package. The AMBER ff14SB force field[63] was used for the proteins and ions. The TIP3P model[50] was used for water molecules. The atomic partial charges of the phosphorylated aspartate were determined by quantum calculation using GAMESS[64] and the RESP[65] charge calculation. The other parameters (bond, angle, and dihedral) of the atoms were obtained using the general Amber force field (GAFF)[66]. These parameter files were generated by the module Antechamber of the AMBER package. The covalent bonds involving hydrogens were constrained using the SHAKE algorithm[67], and the water molecules were kept rigid using the SETTLE algorithm[68]. After a 4000-step energy minimization, the system was brought to thermodynamic equilibrium at 300 K and 0.1, 50, or 100 MPa, using a Langevin thermostat[69] and a Monte Carlo barostat. Equations of motion were integrated with a time step of 2 fs. The long-range Coulomb energy was evaluated using the particle mesh Ewald method[70]. The MD simulations were conducted for 1.0 μs for monomeric CheY, monomeric FliM$_N$, and the complex of CheYp and FliM$_N$, respectively. Two pressure conditions of 0.1 and 100 MPa were used for the simulations of monomeric CheY, and three conditions (0.1, 50, and 100 MPa) were employed for monomeric FliM$_N$ and the CheYp–FliM$_N$ complex.

The solvent accessible surface area (SASA) and the excluded volume (V_{ex}; defined as the inside space of SASA) for CheY, FliM$_N$, and the CheYp–FliM$_N$ complex were calculated using the CAVE software package[71]. The calculation of SASA for the interface residues of the CheYp–FliM$_N$ complex and the other analyses were performed using the cpptraj module of the AmberTools 14 Package. The representative MD structures were determined by k-means clustering into five clusters from the last half of each MD trajectory. Secondary structure was assigned by the DSSP program[72]. The isothermal compressibility, κ_T, was obtained as follows[11].

$$\kappa_T = -\frac{1}{V}\left(\frac{\partial V}{\partial p}\right)_T = \frac{\langle V^2\rangle - \langle V^2\rangle}{k_B T\langle V\rangle} \quad (1)$$

where V, p, k_B, and T represent the system volume, pressure, the Boltzmann constant, and the absolute temperature, respectively. The angle bracket here denotes the average over the last half of the simulation. To calculate the density of bulk water, MD simulations with 10,056 water molecules were performed at 300 K and 0.1, 50, and 100 MPa for 100 ns. The average density during the last 50 ns of the MD trajectories were described in the text as the bulk water density.

The free energy difference between two forms of CheY monomers was calculated from the population of the active form P_{active} and inactive form $P_{inactive}$ as $\Delta G_M = \Delta G_{inactive} - \Delta G_{active} = -k_B T \ln\left(\frac{P_{inactive}}{P_{active}}\right)$. The two forms were distinguished by the χ_1 angle of Y106; the inactive form corresponds to the range from −45° to 135°, the active form corresponds to the other range.

Dissociation simulation of the CheYp–FliM$_N$ complex by PaCS-MD. To observe the dissociation process of the aCheYp and FliM$_N$ complex, we used a PaCS-MD simulation[27,28] in which mutually-overlapping conformational trajectories are generated by cycles of parallel short MD simulations and selection of MD snapshots closer to dissociation without applying additional bias to the system. In earlier works, PaCS-MD was successful in generating natural dissociation pathways of tri-N-acetyl-d-glucosamine from hen egg white lysozyme[31] and those of the transactivation domain of the p53 protein from the MDM2 protein[29]. In the present work, the dissociation process of the complex was investigated by a procedure similar to that used in the earlier reports.

As the initial structures for PaCS-MD, the structures of the CheYp–FliM$_N$ complex after 200 ns MD at 0.1, 50, and 100 MPa were adopted. To observe the dissociation up to $d = 50$ Å, the simulation box was expanded to a cubic box of $83 \times 83 \times 83$ Å^3 and the gaps were filled with water and 0.15 M KCl. The total numbers of atoms in the systems were ~ 56,000 atoms including water and ions. After a short energy minimization, the simulation system was equilibrated at 300 K and 0.1 (or 50 or 100) MPa for 10 ns. The dissociation simulation was conducted five times with different initial conformations selected every 1 ns from the last snapshot of the 10-ns MD trajectory. For each PaCS-MD cycle, ten 100-ps MD simulations were performed in parallel and the trajectories were recorded every 10 fs. The snapshots sampled every 1 ps were rank-ordered according to the inter-COM distance, d, between CheYp and the helical segment of FliM$_N$ (residues 8–16), and the top ten snapshots were selected for the next cycle. The first 7 residues of FliM$_N$ were excluded from the calculation of COM because we noticed in preliminary trials that this region is very flexible and its fluctuation creates 'noise' in detecting the dissociation; the inclusion of the flexible region made detection of the dissociative movements more difficult. This restriction was applied only in the selection in PaCS-MD; all residues of FliM$_N$ were considered for the calculation of the inter-COM distances in other determinations. No positional restraints were applied, thereby allowing reorientation of CheYp. In the present work, we used a larger cubic box so that FliM$_N$ was permitted to dissociate in any direction. This approach differed from that used in the earlier work, in which reorientation of a protein was restrained within a rectangular box[12].

Calculation of binding free energy by MSM. Standard binding free energies of CheYp and FliM$_N$ at pressures of 0.1, 50, and 100 MPa were calculated using the MSM analysis of the MD trajectories[30] generated by each trial. For a reasonable estimation of the transition probabilities among microstates in MSM, the trajectories from 10 independent MD simulations typically were not sufficient to achieve meaningful statistics. Instead, 10 additional MD simulations were performed, starting from the initial structures of each cycle of the PaCS-MD but with different initial velocities. This addition was repeated until sufficient statistics was achieved according to the implied time scale test[30,73]. For the 0.1 MPa condition, one set of the additional MD simulations (10 MDs) was performed for two of the five PaCS-MD trials, and two sets (20 MDs) were performed for the other three trials. At 50 MPa, one additional set (10 MDs) was performed for two trials, three sets (30 MDs) were performed for one trial, and the other two trials were analyzed by MSM without additional MD simulations. At 100 MPa, one additional MD set was performed for four trials, and two sets were performed for the rest.

Clustering and MSM construction were performed for each dissociation simulation using MSMBuilder 3.5.0[74]. The inter-COM distance between CheYp and FliM$_N$ were calculated for all of the snapshots and were clustered into 30 clusters based on the k-means. The same procedure previously was used successfully in reproducing experimentally measured standard binding free energy of a protein-peptide complex[29]. A lag time of 30 ps was selected based on the implied time scales plot as a function of lag time. Free energy profiles (potential of mean force) were first calculated from the stationary probabilities of the microstates of each trial and then averaged over the multiple trials. The bound state was defined as a region before the free energy curve became flat, i.e., 40, 40, and 25 Å of the inter-COM distance for 0.1, 50 and 100 MPa, respectively. The other region (i.e., up to 50 Å after the energy curve became flat) was defined as the unbound state. The free energy difference (ΔG_{bind}) was calculated from the probabilities of the bound (P_b) and unbound (P_u) states:

$$\Delta G_{bind} = -k_B T \ln \frac{P_b}{P_u}, \tag{2}$$

where k_B is the Boltzmann constant and T is the absolute temperature. The values of P_b and P_u were obtained by summing the probabilities of the microstates included in the respective state. The standard free energy of binding (ΔG°_{bind}) was calculated using the following expression with a volume correction term[75]:

$$\Delta G^\circ_{bind} = -\Delta W - k_B T \ln \frac{V_b}{V^\circ} \tag{3}$$

where V_b is the bound volume and V° is the standard-state volume (1661 Å^3). ΔW is the average free energy value of the unbound state compared to that of the bound state. The value of V_b was calculated as the volume of the convex hull defined by the COM coordinates of FliM$_N$ in the bound state relative to the COM of CheYp at the origin. The convex hull calculation was performed for each dissociation simulation using Qhull[76]. Snapshots sampled every 2 ps were used for the V_b calculation. The averaged value of V_b for each pressure condition was used for the ΔG° calculation.

Motility assay. Bacterial assays were performed using *E. coli* strain SYC12 (*fliC-sticky*, wild type for chemotaxis), a derivative of RP437[77]. SYC12 carries the *fliC*st allele, encoding a 'sticky' mutant FliC filament protein that lacks residues 245–301 of what would otherwise be a 497-residue protein[78]; the mutant protein polymerizes into a filament that readily adheres to hydrophobic surfaces[79]. Following growth, the cells were resuspended in MLM medium (10 mM potassium phosphate (pH 7.0), 0.1 mM EDTA, 10 mM DL-lactate, 0.01 mM methionine) as described previously[80]. The motor rotation at ambient pressure and 40 MPa was recorded at 30 frames per second by high-pressure microscopy[15,38,81]. The pressure was controlled with an accuracy of ±1 MPa. The experimental temperature was maintained at 23 ± 1 °C. After the release of pressure, all cells were removed from the chamber, and the next assay was performed using naïve cells (i.e., cells that had not been exposed previously to high pressure). All assays were repeated with at least three different cultures.

Data availability

The datasets generated during and/or analysed during the current study are available from the corresponding author on reasonable request.

Received: 7 November 2019; Accepted: 27 January 2020;
Published online: 11 February 2020

References

1. Boonyaratanakornkit, B. B., Park, C. B. & Clark, D. S. Pressure effects on intra- and intermolecular interactions within proteins. *Biochim. Biophys. Acta - Protein Struct. Mol. Enzymol.* **1595**, 235–249 (2002).
2. Heremans, K. & Smeller, L. Protein structure and dynamics at high pressure. *Biochim. Biophys. Acta - Protein Struct. Mol. Enzymol.* **1386**, 353–370 (1998).
3. Mozhaev, V. V., Heremans, K., Frank, J., Masson, P. & Balny, C. High pressure effects on protein structure and function. *Proteins Struct. Funct. Genet.* **24**, 81–91 (1996).
4. Hata, H., Nishiyama, M. & Kitao, A. Molecular dynamics simulation of proteins under high pressure: Structure, function and thermodynamics. *Biochim. Biophys. Acta - Gen. Subj.* **1864**, 129395 (2020).
5. Heremans, K. High Pressure Effects on Proteins and other Biomolecules. *Annu. Rev. Biophys. Bioeng.* **11**, 1–21 (1982).
6. Zipp, A. & Kauzmann, W. Pressure Denaturation of Metmyoglobin. *Biochem.* **12**, 4217–4228 (1973).
7. Silva, J. L. & Weber, G. Pressure Stability of Proteins. *Annu. Rev. Phys. Chem.* **44**, 89–113 (1993).
8. Hawley, S. A. Reversible Pressure-Temperature Denaturation of Chymotrypsinogen. *Biochem.* **10**, 2436–2442 (1971).
9. Roche, J. & Royer, C. A. Lessons from pressure denaturation of proteins. *J. R. Soc. Interface* **15**, 20180244 (2018).
10. Paci, E. High pressure simulations of biomolecules. *Biochim. Biophys. Acta - Protein Struct. Mol. Enzymol.* **1595**, 185–200 (2002).
11. Wakai, N., Takemura, K., Morita, T. & Kitao, A. Mechanism of Deep-Sea Fish α-Actin Pressure Tolerance Investigated by Molecular Dynamics Simulations. *PLoS One* **9**, e85852 (2014).
12. Fujii, S. *et al*. Commonly stabilized cytochromes c from deep-sea Shewanella and Pseudomonas. *Biosci. Biotechnol. Biochem.* **82**, 792–799 (2018).
13. Okuno, D., Nishiyama, M. & Noji, H. Single-Molecule Analysis of the Rotation of F1-ATPase under High Hydrostatic Pressure. *Biophys. J.* **106**, 393a (2014).
14. Hayashi, M. *et al*. Reversible Morphological Control of Tubulin-Encapsulating Giant Liposomes by Hydrostatic Pressure. *Langmuir* **32**, 3794–3802 (2016).
15. Nishiyama, M. *et al*. High hydrostatic pressure induces counterclockwise to clockwise reversals of the Escherichia coli flagellar motor. *J. Bacteriol.* **195**, 1809–1814 (2013).
16. Morita, T. Structure-based analysis of high pressure adaptation of α-actin. *J. Biol. Chem.* **278**, 28060–28066 (2003).
17. Gross, M. & Jaenicke, R. Proteins under pressure: The influence of high hydrostatic pressure on structure, function and assembly of proteins and protein complexes. *Eur. J. Biochem.* **221**, 617–630 (1994).
18. Karplus, M. & McCammon, A. Molecular dynamics simulations of biomolecules. *Nat. Struct. Biol.* **9**, 646–652 (2002).
19. van Gunsteren, W. F. & Berendsen, H. J. C. Computer Simulation of Molecular Dynamics: Methodology, Applications, and Perspectives in Chemistry. *Angew. Chem. Int. Ed. Engl.* **29**, 992–1023 (1990).
20. Dror, R. O., Dirks, R. M., Grossman, J. P., Xu, H. & Shaw, D. E. Biomolecular Simulation: A Computational Microscope for Molecular Biology. *Annu. Rev. Biophys.* **41**, 429–452 (2012).
21. Smolin, N. & Winter, R. A molecular dynamics simulation of SNase and its hydration shell at high temperature and high pressure. *Biochim. Biophys. Acta - Proteins Proteom.* **1764**, 522–534 (2006).
22. Kitchen, D. B., Reed, L. H. & Levy, R. M. Molecular Dynamics Simulation of Solvated Protein at High Pressure. *Biochem.* **31**, 10083–10093 (1992).
23. Russo, D., Laloni, A., Filabozzi, A. & Heyden, M. Pressure effects on collective density fluctuations in water and protein solutions. *Proc. Natl. Acad. Sci.* **114**, 11410–11415 (2017).
24. Imai, T. & Sugita, Y. Dynamic correlation between pressure-induced protein structural transition and water penetration. *J. Phys. Chem. B* **114**, 2281–2286 (2010).
25. Mori, Y. & Okamoto, Y. Conformational changes of ubiquitin under high pressure conditions: A pressure simulated tempering molecular dynamics study. *J. Comput. Chem.* **38**, 1167–1173 (2017).
26. Trzesniak, D., Lins, R. D. & van Gunsteren, W. F. Protein under pressure: Molecular dynamics simulation of the arc repressor. *Proteins Struct. Funct. Bioinforma.* **65**, 136–144 (2006).
27. Harada, R. & Kitao, A. Parallel cascade selection molecular dynamics (PaCS-MD) to generate conformational transition pathway. *J. Chem. Phys.* **139**, 035103 (2013).
28. Harada, R. & Kitao, A. Nontargeted Parallel Cascade Selection Molecular Dynamics for Enhancing the Conformational Sampling of Proteins. *J. Chem. Theory Comput.* **11**, 5493–5502 (2015).
29. Tran, D. P. & Kitao, A. Dissociation Process of a MDM2/p53 Complex Investigated by Parallel Cascade Selection Molecular Dynamics and the Markov State Model. *J. Phys. Chem. B* **123**, 2469–2478 (2019).
30. Prinz, J.-H. *et al*. Markov models of molecular kinetics: Generation and validation. *J. Chem. Phys.* **134**, 174105 (2011).
31. Tran, D. P., Takemura, K., Kuwata, K. & Kitao, A. Protein–Ligand Dissociation Simulated by Parallel Cascade Selection Molecular Dynamics. *J. Chem. Theory Comput.* **14**, 404–417 (2018).
32. Welch, M., Oosawa, K., Aizawa, S. & Eisenbach, M. Phosphorylation-dependent binding of a signal molecule to the flagellar switch of bacteria. *Proc. Natl. Acad. Sci.* **90**, 8787–8791 (1993).
33. Bren, A. & Eisenbach, M. The N terminus of the flagellar switch protein, FliM, is the binding domain for the chemotactic response regulator, CheY. *J. Mol. Biol.* **278**, 507–514 (1998).

34. Larsen, S. H., Reader, R. W., Kort, E. N., Tso, W. W. & Adler, J. Change in direction of flagellar rotation is the basis of the chemotactic response in Escherichia coli. *Nat.* **249**, 74–77 (1974).
35. Bai, F. *et al*. Conformational spread as a mechanism for cooperativity in the bacterial flagellar switch. *Sci.* **327**, 685–689 (2010).
36. Wang, F. *et al*. Non-equilibrium effect in the allosteric regulation of the bacterial flagellar switch. *Nat. Phys.* **13**, 710–714 (2017).
37. Bai, F., Minamino, T., Wu, Z., Namba, K. & Xing, J. Coupling between Switching Regulation and Torque Generation in Bacterial Flagellar Motor. *Phys. Rev. Lett.* **108**, 178105 (2012).
38. Nishiyama, M. & Sowa, Y. Microscopic analysis of bacterial motility at high pressure. *Biophys. J.* **102**, 1872–1880 (2012).
39. Lee, S. Y. *et al*. Crystal structure of an activated response regulator bound to its target. *Nat. Struct. Biol.* **8**, 52–56 (2001).
40. Volz, K. & Matsumura, P. Crystal structure of *Escherichia coli* CheY refined at 1.7-Å resolution. *J. Biol. Chem.* **266**, 15511–15519 (1991).
41. Dyer, C. M. *et al*. Structure of the constitutively active double mutant CheY D13K Y106W alone and in complex with a FliM peptide. *J. Mol. Biol.* **342**, 1325–1335 (2004).
42. Halkides, C. J. *et al*. The 1.9 Å resolution crystal structure of phosphono-CheY, an analogue of the active form of the response regulator, CheY. *Biochem.* **39**, 5280–5286 (2000).
43. Welch, M., Eisenbach, M., Oosawa, K. & Aizawa, S. I. Effects of Phosphorylation, Mg^{2+}, and Conformation of the Chemotaxis Protein CheY on Its Binding to the Flagellar Switch Protein FliM. *Biochem.* **33**, 10470–10476 (1994).
44. McEvoy, M. M., Bren, A., Eisenbach, M. & Dahlquist, F. W. Identification of the binding interfaces on CheY for two of its targets the phosphatase CheZ and the flagellar switch protein FliM. *J. Mol. Biol.* **289**, 1423–1433 (1999).
45. Calandrini, V. *et al*. Relaxation dynamics of lysozyme in solution under pressure: Combining molecular dynamics simulations and quasielastic neutron scattering. *Chem. Phys.* **345**, 289–297 (2008).
46. Erlkamp, M. *et al*. Influence of Pressure and Crowding on the Sub-Nanosecond Dynamics of Globular Proteins. *J. Phys. Chem. B* **119**, 4842–4848 (2015).
47. Appavou, M.-S., Gibrat, G. & Bellissent-Funel, M.-C. Influence of pressure on structure and dynamics of bovine pancreatic trypsin inhibitor (BPTI): Small angle and quasi-elastic neutron scattering studies. *Biochim. Biophys. Acta - Proteins Proteom.* **1764**, 414–423 (2006).
48. Nishima, W., Qi, G., Hayward, S. & Kitao, A. DTA: Dihedral transition analysis for characterization of the effects of large main-chain dihedral changes in proteins. *Bioinforma.* **25**, 628–635 (2009).
49. Nishiyama, M. High-pressure microscopy for tracking dynamic properties of molecular machines. *Biophys. Chem.* **231**, 71–78 (2017).
50. Jorgensen, W. L., Chandrasekhar, J., Madura, J. D., Impey, R. W. & Klein, M. L. Comparison of simple potential functions for simulating liquid water. *J. Chem. Phys.* **79**, 926–935 (1983).
51. Pereira, B., Jain, S., Sarupria, S., Yang, L. & Garde, S. Pressure dependence of the compressibility of a micelle and a protein: Insights from cavity formation analysis. *Mol. Phys.* **105**, 189–199 (2007).
52. Chalikian, T. V. & Breslauer, K. J. Thermodynamic analysis of biomolecules: A volumetric approach. *Curr. Opin. Struct. Biol.* **8**, 657–664 (1998).
53. Kojima, H., Ishijima, A. & Yanagida, T. Direct measurement of stiffness of single actin filaments with and without tropomyosin by *in vitro* nanomanipulation. *Proc. Natl. Acad. Sci.* **91**, 12962–12966 (1994).
54. Sowa, Y. & Berry, R. M. Bacterial flagellar motor. *Q. Rev. Biophys.* **41**, 103–132 (2008).
55. Duke, T. A. J., Le Novère, N. & Bray, D. Conformational spread in a ring of proteins: a stochastic approach to allostery. *J. Mol. Biol.* **308**, 541–553 (2001).
56. Paul, K., Brunstetter, D., Titen, S. & Blair, D. F. A molecular mechanism of direction switching in the flagellar motor of Escherichia coli. *Proc. Natl. Acad. Sci.* **108**, 17171–17176 (2011).
57. Sadaie, W., Harada, Y., Matsuda, M. & Aoki, K. Quantitative *In Vivo* Fluorescence Cross-Correlation Analyses Highlight the Importance of Competitive Effects in the Regulation of Protein-Protein Interactions. *Mol. Cell. Biol.* **34**, 3272–3290 (2014).
58. Hummer, G., Garde, S., García, A. E., Paulaitis, M. E. & Pratt, L. R. The pressure dependence of hydrophobic interactions is consistent with the observed pressure denaturation of proteins. *Proc. Natl. Acad. Sci.* **95**, 1552–1555 (1998).
59. Ghosh, T., García, A. E. & Garde, S. Molecular dynamics simulations of pressure effects on hydrophobic interactions. *J. Am. Chem. Soc.* **123**, 10997–11003 (2001).
60. Cheung, J. K., Shah, P. & Truskett, T. M. Heteropolymer Collapse Theory for Protein Folding in the Pressure-Temperature Plane. *Biophys. J.* **91**, 2427–2435 (2006).
61. Levin, A. *et al*. Analyzing protein-ligand and protein-interface interactions using high pressure. *Biophys. Chem.* **252**, 106194 (2019).
62. Götz, A. W. *et al*. Routine Microsecond Molecular Dynamics Simulations with AMBER on GPUs. 1. Generalized Born. *J. Chem. Theory Comput.* **8**, 1542–1555 (2012).
63. Maier, J. A. *et al*. ff14SB: Improving the Accuracy of Protein Side Chain and Backbone Parameters from ff99SB. *J. Chem. Theory Comput.* **11**, 3696–3713 (2015).
64. Schmidt, M. W. *et al*. General atomic and molecular electronic structure system. *J. Comput. Chem.* **14**, 1347–1363 (1993).
65. Bayly, C. I., Cieplak, P., Cornell, W. & Kollman, P. A. A well-behaved electrostatic potential based method using charge restraints for deriving atomic charges: the RESP model. *J. Phys. Chem.* **97**, 10269–10280 (1993).
66. Wang, J., Wolf, R. M., Caldwell, J. W., Kollman, P. A. & Case, D. A. Development and testing of a general amber force field. *J. Comput. Chem.* **25**, 1157–1174 (2004).
67. Ryckaert, J.-P., Ciccotti, G. & Berendsen, H. J. C. Numerical integration of the cartesian equations of motion of a system with constraints: molecular dynamics of n-alkanes. *J. Comput. Phys.* **23**, 327–341 (1977).
68. Miyamoto, S. & Kollman, P. A. Settle: An analytical version of the SHAKE and RATTLE algorithm for rigid water models. *J. Comput. Chem.* **13**, 952–962 (1992).
69. Prusty, M. & Cheong, S. A. Stochastic boundary conditions for molecular dynamics simulations. *Chem. Phys. Lett.* **105**, 495–500 (2009).
70. Essmann, U. *et al*. A smooth particle mesh Ewald method. *J. Chem. Phys.* **103**, 8577–8593 (1995).
71. Buša, J., Hayryan, S., Hu, C.-K., Skřivánek, J. & Wu, M.-C. Cave: A package for detection and quantitative analysis of internal cavities in a system of overlapping balls: Application to proteins. *Comput. Phys. Commun.* **181**, 2116–2125 (2010).
72. Kabsch, W. & Sander, C. Dictionary of protein secondary structure: Pattern recognition of hydrogen-bonded and geometrical features. *Biopolym.* **22**, 2577–2637 (1983).
73. Trendelkamp-Schroer, B. & Noé, F. Efficient Estimation of Rare-Event Kinetics. *Phys. Rev. X* **6**, 011009 (2016).
74. Beauchamp, K. A. *et al*. MSMBuilder2: Modeling Conformational Dynamics on the Picosecond to Millisecond Scale. *J. Chem. Theory Comput.* **7**, 3412–3419 (2011).
75. Buch, I., Giorgino, T. & De Fabritiis, G. Complete reconstruction of an enzyme-inhibitor binding process by molecular dynamics simulations. *Proc. Natl. Acad. Sci.* **108**, 10184–10189 (2011).
76. Barber, C. B., Dobkin, D. P. & Huhdanpaa, H. The quickhull algorithm for convex hulls. *ACM Trans. Math. Softw.* **22**, 469–483 (1996).
77. Parkinson, J. S. Complementation analysis and deletion mapping of Escherichia coli mutants defective in chemotaxis. *J. Bacteriol.* **135**, 45–53 (1978).
78. Kuwajima, G. Construction of a minimum-size functional flagellin of Escherichia coli. *J. Bacteriol.* **170**, 3305–3309 (1988).

79. Berg, H. C. & Turner, L. Torque generated by the flagellar motor of Escherichia coli. *Biophys. J.* **65**, 2201–2216 (1993).
80. Nishiyama, S., Umemura, T., Nara, T., Homma, M. & Kawagishi, I. Conversion of a bacterial warm sensor to a cold sensor by methylation of a single residue in the presence of an attractant. *Mol. Microbiol.* **32**, 357–365 (1999).
81. Nishiyama, M. & Arai, Y. Tracking the Movement of a Single Prokaryotic Cell in Extreme Environmental Conditions. In 175–184 (Humana Press, New York, NY, 2017). https://doi.org/10.1007/978-1-4939-6927-2_13
82. Humphrey, W., Dalke, A. & Schulten, K. VMD: Visual molecular dynamics. *J. Mol. Graph.* **14**, 33–38 (1996).

Acknowledgements

We thank Dr. Yong-Suk Che for providing *E. coli* strain SYC12. This research was supported in part by MEXT/JSPS KAKENHI grants to I.K., M.N., and A.K. (No. JP17KT0026), to A.K. (No. JP19H03191), to M.N. (Nos. JP16K04908 and JP17H05880), and to Y.S. (No. JP19H05404), and by a MEXT grant ("Priority Issue on Post-K Computer" (Building Innovative Drug Discovery Infrastructure Through Functional Control of Biomolecular Systems)) to A.K. The computations were performed in part using the supercomputers at The Research Center for Computational Science (RCCS), The National Institute of Natural Science, and at The Institute of Solid State Physics (ISSP), The University of Tokyo. This research also used computational resources of the K computer provided by the RIKEN Advanced Institute for Computational Science through the HPCI System Research project (Project IDs: hp150270, hp160207, hp170254, hp180201, and hp190181).

Author contributions

H.H., Y.N., M.N., Y.S., I.K. and A.K. conceived the study. H.H., Y.N. and A.K. conducted computations. M.N., Y.S. and I.K. conducted experiments. H.H., Y.N., M.N., Y.S., I.K. and A.K. analyzed the results and wrote the manuscript.

Competing interests

The authors declare no competing interests.

Additional information

Supplementary information is available for this paper at https://doi.org/10.1038/s41598-020-59172-3.

Correspondence and requests for materials should be addressed to A.K.

Reprints and permissions information is available at www.nature.com/reprints.

Publisher's note Springer Nature remains neutral with regard to jurisdictional claims in published maps and institutional affiliations.

Open Access This article is licensed under a Creative Commons Attribution 4.0 International License, which permits use, sharing, adaptation, distribution and reproduction in any medium or format, as long as you give appropriate credit to the original author(s) and the source, provide a link to the Creative Commons license, and indicate if changes were made. The images or other third party material in this article are included in the article's Creative Commons license, unless indicated otherwise in a credit line to the material. If material is not included in the article's Creative Commons license and your intended use is not permitted by statutory regulation or exceeds the permitted use, you will need to obtain permission directly from the copyright holder. To view a copy of this license, visit http://creativecommons.org/licenses/by/4.0/.

© The Author(s) 2020